UC Office of the President
Recent Work

Title

Development and Translation of PEDOT: PSS Microelectrodes for Intraoperative Monitoring

Permalink

https://escholarship.org/uc/item/6z58575j

Authors

Ganji, Mehran
Kaestner, Erik
Hermiz, John
et al.

Publication Date

2017

Peer reviewed

Development and Translation of PEDOT:PSS Microelectrodes for Intraoperative Monitoring

Mehran Ganji, Erik Kaestner, John Hermiz, Nick Rogers, Atsunori Tanaka, Daniel Cleary, Sang Heon Lee, Jospeh Snider, Milan Halgren, Garth Rees Cosgrove, Bob S. Carter, David Barba, Ilke Uguz, George G. Malliaras, Sydney S. Cash, Vikash Gilja,* Eric Halgren,* and Shadi A. Dayeh*

Recording neural activity during neurosurgical interventions is an invaluable tool for both improving patient outcomes and advancing our understanding of neural mechanisms and organization. However, increasing clinical electrodes' signal-to-noise and spatial specificity requires overcoming substantial physical barriers due to the compromised metal electrochemical interface properties. The electrochemical properties of poly(3,4-ethylenedioxythiophene):poly(styrenesulfonate) (PEDOT:PSS) based interfaces surpass those of current clinical electrocorticography electrodes. Here, robust fabrication process of PEDOT:PSS microelectrode arrays is demonstrated for safe and high fidelity intraoperative monitoring of human brain. PEDOT:PSS microelectrodes measure significant differential neural modulation under various clinically relevant conditions. This study reports the first evoked (stimulus-locked) cognitive activity with changes in amplitude across pial surface distances as small as 400 μm, potentially enabling basic neurophysiology studies at the scale of neural micro-circuitry.

1. Introduction

Electrocorticography (ECoG) is preferred in clinical and experimental mapping of brain activity due to its higher spatial resolution and sensitivity compared to electroencephalography (EEG) and magnetoencephalography (MEG), yet retains their greater temporal resolution compared to functional magnetic resonance imaging (fMRI).[1] In the clinical context, ECoG is used for precise localization of eloquent cortex in neurosurgical cases for tumors, epileptogenic foci, and vascular abnormalities. This functional localization can be confirmed using ECoG electrodes by electrical stimulation producing a temporary, functional lesion. In the experimental context, most clinical ECoG can resolve activity to less than a millimeter with a high degree of certainty, relative to fMRI, MEG, and EEG,[2] which rely upon modeling and reconstruction techniques to estimate signal source locations. Furthermore, ECoG can measure not only field potentials (which like MEG and EEG are mainly due to currents in the apical dendrites of pyramidal cells), but also measure high-frequency power, which reflects neuronal population firing.[3] Consequently, the use of ECoG in clinical environments is critical for improving neurosurgical patient outcomes—estimated to be 111, 00 patient

M. Ganji, J. Hermiz, S. H. Lee, Prof. V. Gilja, Prof. S. A. Dayeh
Department of Electrical and Computer Engineering
University of California San Diego
La Jolla, CA 92093, USA
E-mail: vgilja@eng.ucsd.edu; sdayeh@eng.ucsd.edu
E. Kaestner, Prof. V. Gilja, Prof. E. Halgren
Neurosciences Program
University of California San Diego
La Jolla, CA 92096, USA
E-mail: halgren@ucsd.edu
N. Rogers, Dr. J. Snider
Department of Physics
University of California San Diego
La Jolla, CA 92161, USA
A. Tanaka, Prof. S. A. Dayeh
Materials Science and Engineering Program
University of California San Diego
La Jolla, CA 92093, USA
Dr. D. Cleary, Dr. B. S. Carter, Dr. D. Barba
Department of Neurosurgery
University of California San Diego
La Jolla, CA 92103, USA

M. Halgren, Dr. S. S. Cash
Department of Neurology
Massachusetts General Hospital
Boston, MA 02114, USA
Dr. G. R. Cosgrove
Neurosurgery
Brigham and Women's Hospital
Boston, MA 02115, USA
Dr. I. Uguz, Prof. G. G. Malliaras
Department of Bioelectronics
CMP-EMSE
MOC
13541 Gardanne, France
Prof. E. Halgren
Department of Radiology
University of California San Diego
La Jolla, CA 92103, USA
Prof. S. A. Dayeh
Department of NanoEngineering
University of California San Diego
La Jolla, CA 92093, USA

ADVANCED
SCIENCE NEWS
www.advancedsciencenews.com

ADVANCED
FUNCTIONAL
MATERIALS
www.afm-journal.de

cases per year in the US only[4]—for localizing a wide variety of cortical task-related activity, and for implementing brain-machine interfaces (BCI).[1,5]

However, current clinical ECoG electrodes face physical limits to the number of electrode sites, spatial resolution (centimeter scale), and electrode diameter (millimeter scale), and thus cannot resolve neural activity that changes multiple times over the course of a millimeter.[6] This limitation has important implications for surgical tissue resection, as current surgical methodology requires high precision in identifying the boundaries between diseased and eloquent cortex. In addition to these design limitations, current clinical electrode arrays are constrained to nonconformal electrode-carriers/substrates and to less-optimal metal (e.g., PtIr) electrochemical interfaces.[7] To fully exploit the advantages of ECoG in both clinical and experimental mapping of detailed neural activity, significant advances at the electrochemical, mechanical and biocompatibility fronts of electrode/tissue interfaces must be made.[8] The needed advances includes (1) the development of a high-quality electrochemical interface with low impedance (high signal-to-noise ratio (SNR) recording), (2) high charge injection capacity (safe/efficient stimulation),[9] (3) compliant mechanical properties for mimicking the curvilinear brain surface and to compensate for brain micromotion in order to reduce tissue damage,[10] and (4) enhanced biocompatible electrode/tissue interfaces to minimize biofouling.[8a,11]

Here we focus on the development of high-SNR neural recordings to increase the spatial specificity at which neural activity can be measured. Several novel materials and strategies have been employed, focusing on increasing SNR by lowering electrode impedance. Nanostructured materials such as nanowires, carbon nanotubes and graphene[12] as well as surface-modified metallic electrodes (Pt, Au, and Ir) with porous surfaces and higher geometrical surface area are among those explored.[9b,13] Their fabrication processes are generally not monolithic and face additional challenges for translation to clinical practice than poly(3,4-ethylenedioxythiophene) (PEDOT). For metallic electrodes, their relatively high electrochemical impedances and site-to-site variability can result in significant electrophysiological recording losses.

Conductive polymers (CPs) on the other hand offer excellent possibilities for advancing electrode/tissue interfaces. CPs have significantly lower microelectrode impedance than inorganic microelectrodes due to their combined ionic-electronic conductivity.[14] In addition, by minimizing the mechanical mismatch at electrode/tissue interface, they permit long-lasting functional neural interface[15] with diminished biofouling.[16] When built on thin flexible films of polyimide or parylene, they conform to the curvilinear brain tissue[17] and their transparency permits their accurate placement on the cortical surface in desired regions. In particular, PEDOT:poly(styrenesulfonate) (PSS) is considered as a forefront alternative due to its low electrochemical impedance over a wide range of frequencies of cortical activity that is of interest,[14,18] its excellent chemical stability,[19] and its biocompatibility.[20] However, to date, there is only one group who has demostrated PEDOT:PSS utilization in intraoperative monitoring. Their pioneering work reported single units from a human brain and began to explore the spatial specificity capabilities of PEDOT:PSS devices.[21] Here we expand on these

efforts by thoroughly benchmarking PEDOT:PSS electrodes against clinical electrodes and by demonstrating background, functional, and pathological recordings, the complete suite of mapping that is necessary for clinical translation of PEDOT:PSS into intraoperative monitoring.

The objective of our work is to advance PEDOT:PSS microelectrode arrays for high fidelity electrophysiological recordings in human subjects. To accomplish this, we first studied the structural and surface integrity of the devices for suitability in safe intraoperative monitoring from human subjects. Here, we refined earlier fabrication procedures[22] for which we optimized the autoclave sterilization for clinical use,[23] and obtained high yield with a narrow distribution of microelectrode electrochemical characteristics. We benchmark PEDOT:PSS electrodes characteristics against clinical PtIr and pure Pt electrodes, correlate clinical recordings from PEDOT:PSS and clinical electrodes to their electrochemical properties, and present the first recording of stimulus-locked neural activity from human subjects using PEDOT:PSS microarrays. By employing high yield PEDOT:PSS microelectrode arrays, not only high SNR was obtained, but evidence of spatially modulated activity across the scale of cortical microcolumns was measured. These changes, measured in high-gamma amplitude across 400 µm pitch electrodes, demonstrate the spatial specifity afforded by the low impedance, small electrode diameter, and fine electrode pitch of the fabricated PEDOT:PSS devices.

2. Results

2.1. Device Benchmarking

To realize the fully conformal, high-density PEDOT:PSS microelectrode array, we utilized parylene C as an insulating and flexible substrate carrier for the sensing electrodes and the metalization lines. The device consisted of an array of 56 microelectrodes (arranged in an 8 × 7 grid) and 6 macrodots (arranged in a 1 × 6 strip) of which a subset was used as reference. The macrodots have the same 3 mm diameter as commonly used clinical electrodes (e.g., Ad-Tech Medical Inc.) and are arranged in the same form factor (strip shape with 1 cm spacing) as shown in **Figure 1**a. The microelectrodes have 50 µm diameter microdots and are spaced 400 µm center-to-center yielding an array that has a footprint of 3.25 mm × 2.85 mm. Extension to higher density and channel counts is possible with either passive wiring[21a] or active multiplexing electronics,[24] here we focus on the clinical translation of PEDOT:PSS by recording µECoG intraoperatively. We use this design to directly compare clinical recordings obtained by standard PtIr electrodes, similarly sized PEDOT:PSS macrodots, and the scaled PEDOT:PSS microdot arrays.

The fabrication process on 4″ glass carrier wafers is discussed in detail in the experimental section. Figure 1b–d show optical microscope images of the microarray after Ti/Au 10 nm/100 nm evaporation, parylene C chemical vapor deposition and selective etching above the Ti/Au microdots, and definition of PEDOT:PSS only above the Ti/Au microcontacts by a spin-cast and peel-off process. The metal leads are encasulated with ≈2.9 µm thick parylene C from each side. Therefore, the
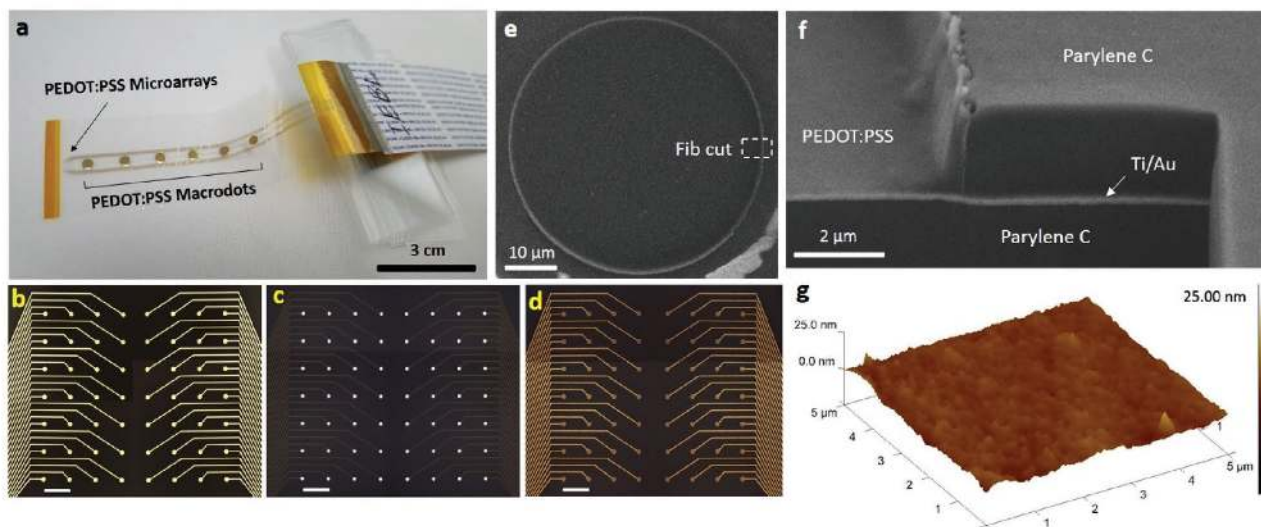
Figure 1. Structural and morphological characterization of PEDOT:PSS electrophysiology device. a) A picture of the fabricated electrophysiology PEDOT:PSS device on thin film parylene C layer showing the location of microarrays with 56 microdots at the top of the probe and above the 6 macro REF electrodes. Optical microscope image of the microelectrodes after b) Ti/Au deposition and lift-off process, c) selective parylene C oxygen plasma etching to expose the gold electrodes, and d) definition of PEDOT:PSS layer on top of only the metal microelectrode sites (scale bars 400 μm). e) Top view SEM image of the circular PEDOT:PSS microelectrode with 50 μm diameter. The white contrast in the lower right of the image is the result of electron charging on parylene C and does not signify a morphological detail. The dashed white box highlights the location of FIB cut. f) Slanted view SEM image showing the cross-section of the device and the stacked layers highlighting conformal and intimate contact between the different layers of the device and exposure of PEDOT:PSS as the only electrochemical interface. g) 3D AFM topography image of a 5 × 5 μm scan area of PEDOT:PSS film after autoclave sterilization showing smooth and uniform morphology (compared to before sterilization, not shown) and the absence of voids in the film.

cortical surface will only be exposed to the PEDOT microcontacts and the parylene C substrate surface. Figure 1e shows a scanning electron microscope (SEM) image of one 50 μm diameter microdot.

To confirm the structural integrity of the microdots and their interfaces with both parylene C and underlying metal contacts, a critical safety factor for use in clinical procedures, we performed focused-ion-beam (FIB) slicing at the edge of the microdot of Figure 1e. The parylene C layers embed the edges of the metal contact and are etched at its center where only PEDOT:PSS was deposited as shown in Figure 1f. The spin-casting approach for depositing PEDOT:PSS enables an intimate contact with the underlying metal and the sidewall of the etched parylene C, forming a tight and fully biocompatible neural interface device. After autoclave sterilization at 121 °C for 20 min in steam, we performed atomic force microscopy (AFM) on the PEDOT:PSS surface for two purposes: (1) validate that insignificant morphological changes occur post sterilization, and (2) no nanoscale voids exist in the PEDOT itself such that the electrochemical interface is only PEDOT:PSS and not a mixed PEDOT:PSS and metal one as is the case when PEDOT:PSS is electrodeposited on metal contacts. Figure 1g shows the AFM image on PEDOT:PSS film after autoclave showing a relatively smooth and continuous surface with a root mean square surface roughness of 1.22 nm. These cumulative structural studies support the integrity of PEDOT:PSS on parylene C for safe intraoperative monitoring of brain activity.

For high fidelity recordings, the yield and reproducibility in device fabrication is important. Our refined fabrication process (see the Experimental Section) resulted in a high yield of functional microelectrodes (>96% functional) and a

very narrow distribution of their impedances. Specifically, as shown in **Figure 2**a, conventional fabrication procedures lead to a 1 kHz average impedance of 19.81 ± 6.94 kΩ whereas the refined procedure for three separate devices resulted in average impedances of 12.68 ± 0.35, 12.12 ± 0.4, and 13.1 ± 0.45 kΩ (Figure 2a). Since clinical electrodes are not manufactured with microscale electrodes, we fabricated a comparison set of Pt microarrays in a similar fashion to our PEDOT:PSS arrays to compare impedance profiles. In contrast to PEDOT:PSS devices, Pt microelectrodes demonstrated a broader distribution of impedances with average impedance at 1 kHz of 337.52 ± 37.02, 290.23 ± 35.2, and 316.64 ± 27.18 kΩ (Figure 2b). The Bode plots of the electrochemical impedance spectroscopy (EIS) for one of these device types (MGS-112 with PEDOT:PSS contacts) and (Pt3 with platinum contacts) are depicted in the inset of Figure 2a,b respectively and demonstrate nearly identical electrochemical characteristics for all of 56 PEDOT:PSS microdots and nonuniform characteristics for Pt microdots in the array. EIS characterization of Pt and PEDOT:PSS micro/macro electrodes are shown in Figure 2c,d (clinical electrode EIS spectra are shown in Figure S2, Supporting Information). The impedance of PEDOT:PSS microarrays (50 μm diameter) displayed mostly capacitive characteristics below 100 Hz; above 100 Hz the impedance saturates at the series resistance values in a regime where the electrochemical current is impeded by edge current crowding and solution resistance. Across frequencies of interest for physiological analyses (1 Hz–10 kHz), PEDOT:PSS microelectrodes exhibited more than ten times lower impedances than those measured for Pt microelectrodes. The impedance of Pt microarrays on the other hand displayed a nearly fixed dependence on frequency with mixed capacitive
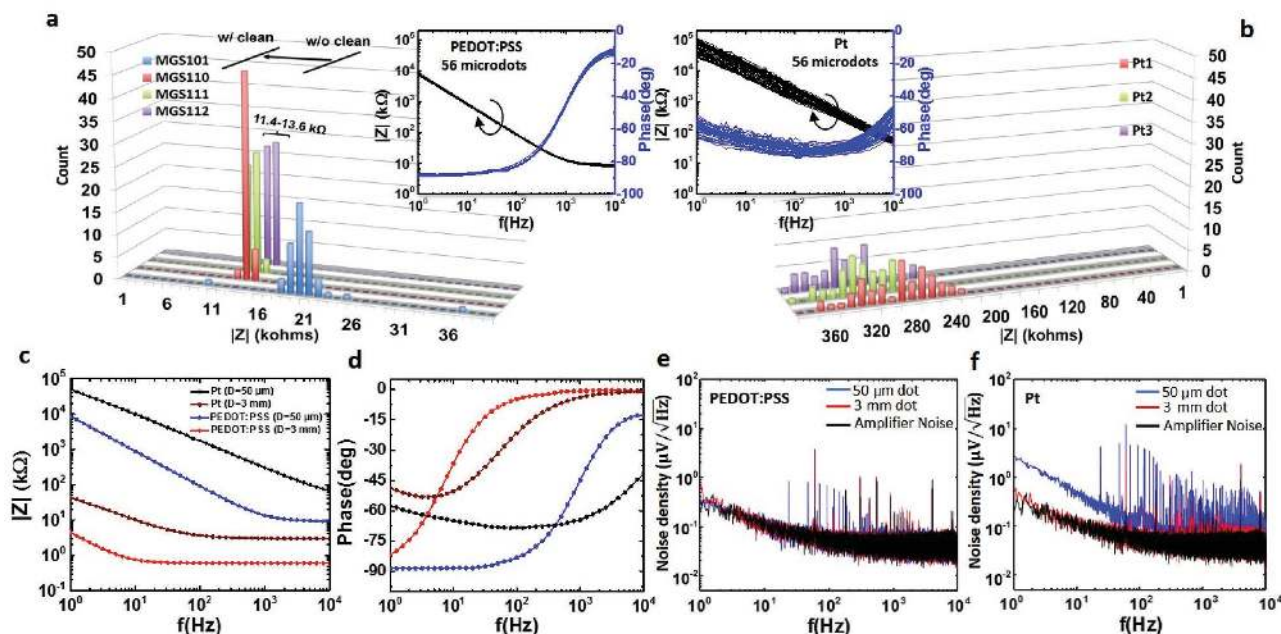
Figure 2. Electrochemical comparison of platinum and PEDOT:PSS electrodes. a) The 1 kHz impedance histogram for three optimized PEDOT:PSS devices, i.e., MGS 110, MGS 111, and MGS 112, with 55, 54, and 56 working channels out of 56 microdots, respectively, and for the nonoptimized PEDOT:PSS (MGS 101). b) The 1 kHz impedance histogram for three Pt devices, i.e., Pt1, Pt2, and Pt3 with 52, 54, and 56 working channels out of 56 microdots, respectively. The insets of (a) and (b) show EIS spectra for all 56 microdots of MGS 112 and Pt3 displaying robust and uniform characteristics of PEDOT:PSS microdots compared to nonuniformity of Pt microdots. c) Impedance and d) phase spectra for micro and macro PEDOT:PSS and Pt electrodes showing distinctive electrochemical behavior (see the text) and lower impedances for PEDOT:PSS. e) The noise density of micro/macro PEDOT:PSS and f) Pt electrodes showing that PEDOT:PSS noise is low and is masked by the amplifier noise whereas Pt microdot noise is significantly higher, particularly in the low-frequency regime (theta, gamma, and low-frequency oscillation bands) where cognitive field potentials are located.

and faradaic processes. For the larger 3 mm diameter macrodots, the impedances become significantly lower and are dominated by series resistances (detailed models with size dependencies will be published elsewhere[25]). These impedance values dictate the noise spectra shown in Figure 2e,f. The relatively low impedance PEDOT micro and macrodots and the Pt macrodot all exhibit noise power spectral density that is similar to that of the amplifier. The smaller Pt microelectrode with over one order of magnitude higher impedance than the PEDOT microelectrodes exhibit a larger noise floor than all other electrodes and the amplifier noise. These uniform impedances and lower noise spectra for PEDOT microelectrodes compared to Pt microelectrodes highlight their potential for scaled ECoG microelectrodes without compromising the signal to noise ratio, as we validate in this work.

2.2. Human Electrocorticography

Having shown the favorable characteristics of our PEDOT:PSS electrodes compared to Pt electrodes, next we assessed our electrodes' ability to measure human electrophysiological activity. We performed intraoperative recordings in both anesthetized patients and patients undergoing clinical mapping of eloquent cortex during epilepsy and tumor resection surgery. The recordings reported consist of testing with four individuals: three at UC San Diego (UCSD) Thornton Hospital (La Jolla, CA) and one at Brigham and Women's (BW) Hospital (Boston, MA). At

UCSD, we performed recordings using PEDOT:PSS from Subject 1 (S1) both while awake and while unconscious, and from Subjects 2 and 3 (S2 and S3) while performing a cognitive task. At BW, Subject 4 (S4) was unconscious during the recordings.

As an initial analysis, we demonstrate that PEDOT records comparable activity to current clinical electrodes (**Figure 3**). Here we compare electrophysiology from the macrodot Pt (clinical electrodes), versus the macrodot and microdot PEDOT:PSS electrodes during two different states for S1 when the electrodes were implanted on the anterior superior temporal gyrus (STG). The first state is awake and is engaged in an audio-visual task (see the Experimental Section for details) versus the second state of anesthesia with Propofol and Dexmedetomidine. As expected there were readily observable differences in electrophysiological recordings between the two states as illustrated in power spectral densities (PSD) (Figure 3a–c), time–frequency plots and time series (Figure 3d–g). There is markedly higher power in the anesthetized condition and in particular in the 12–17 Hz range, indicative of spindle-like activity (Figure 3a–c). Spindling has been reported in deeply anesthetized patients under the drug Dexmedetomidine.[26] Time–frequency plots also appear to show spindling and other dynamic neural activity (Figure 3d,e). Clinical ECoG using standard of care electrodes (3 mm Pt) were recorded alongside PEDOT ECoG. A PSD of a clinical electrode shows comparable effects to those measured by the PEDOT electrodes: (1) increased power during the anesthetized condition and (2) a prominent peak around the alpha range for the task condition. Each electrode showed a significant
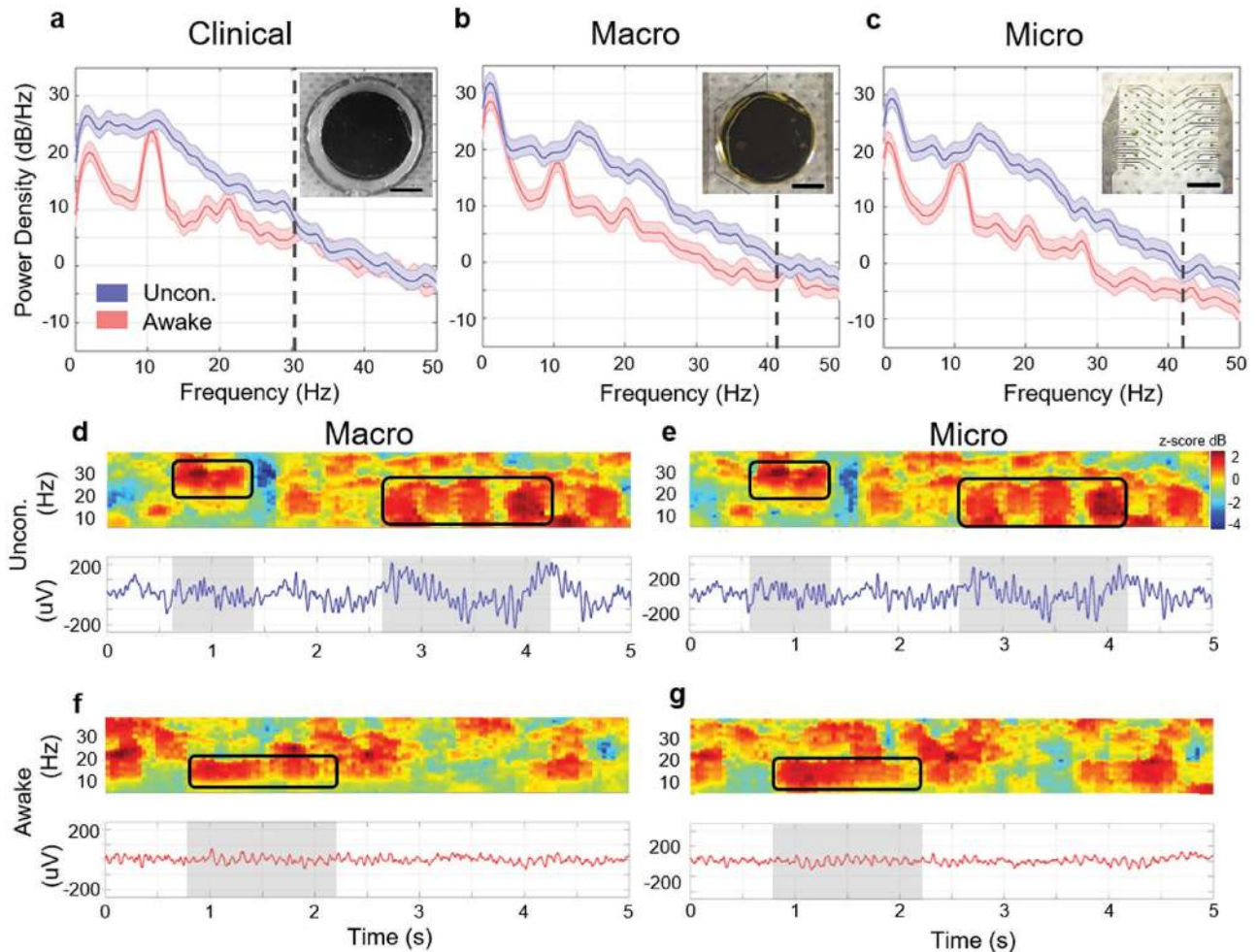
**ADVANCED
SCIENCE NEWS**
www.advancedsciencenews.com

**ADVANCED
FUNCTIONAL
MATERIALS**
www.afm-journal.de

Figure 3. Awake versus unconscious ECoG differences in clinical, PEDOT macro, and micro electrodes. Power spectral densities (PSDs) between the two conditions (awake vs unconscious) for a) clinical electrode, b) PEDOT macro, and c) microdot. Inset of (a) shows optical image of clinical Pt macrodot and panels (b) and (c) show optical image of PEDOT:PSS macrodot and an array of 56 microdots (scale bars 1 mm). The dark blue and red lines are average PSD estimates from overlapping time windows and the lightly colored shaded regions are the 95% pointwise c.i. (see the Experimental Section). Power over the 10–50 Hz band shows significant differences between the two conditions for all electrodes: 8.9×10^{-5} (clinical), 1×10^{-4} (macro), and 8.9×10^{-5} (micro) (Wilcoxon signed rank test). The absolute median difference between 10–50 Hz of the estimate power density is 2.4, 6.2, and 7.8 dB for clinical-, macro-, and microelectrode, respectively. The dashed black line at 30, 42, and 44 Hz for (a)–(c) mark the frequency at which the c.i.s start to overlap for frequencies >15 Hz. Time–frequency and corresponding time series are shown for a sample 5 s window for the unconscious (d and e) and awake condition (f and g). The rectangles highlight increases in beta (20–30 Hz) and spindling activity (12–17 Hz). Color axis represents standard deviations away from the mean for each frequency. The time window per condition for macro and micro are nearly identical.

difference in power in the 10–50 Hz band (Figure 3a–c). However, there is variation in the PSD difference magnitude between the clinical and PEDOT for these measurements. The absolute median difference across 10–50 Hz frequencies is 2.4, 6.2, and 7.8 dB for clinical-, macro-, and microelectrode, respectively. Furthermore, the 95% pointwise confidence intervals (c.i.s) for the two PSD conditions begin to overlap at successively high frequencies: 30, 42, and 44 Hz, for a clinical, macro, and microelectrode, respectively (Figure 3a–c); it is important to note that these simultaneous recordings were made from different cortical sites, centimeters apart, which is likely a source of variation in the measured physiological response across electrode types. The critical observation is that the expected physiological modulation observed in the clinical ECoG is also seen in micro PEDOT electrode.

Another example of consistent physiological effects observed across electrode types is shown in **Figure 4**. S4 was undergoing a standard nondominant temporal lobe resection. Prior to removal, clinical and PEDOT electrodes were placed on the lateral surface of the temporal lobe across the superior and middle temporal gyrus. After recording under usual anesthetic conditions, a dose of Methohexital (Brevital) was administered with the intention of increasing epileptiform activity.[27] As expected, this caused a noticeable increase in epileptiform activity after several minutes as illustrated in the time traces across the electrode types (Figure 4a,b). The time traces are taken over two windows: T_1 which was shortly after the Methohexital dose and T_2 which occurred 200 s after T_1. PSDs for T_1 and T_2 are plotted for clinical, PEDOT macro, and micro (Figure 4c–e, respectively) showing the same trend: more activity in T_2. However,

**ADVANCED
SCIENCE NEWS**

www.advancedsciencenews.com

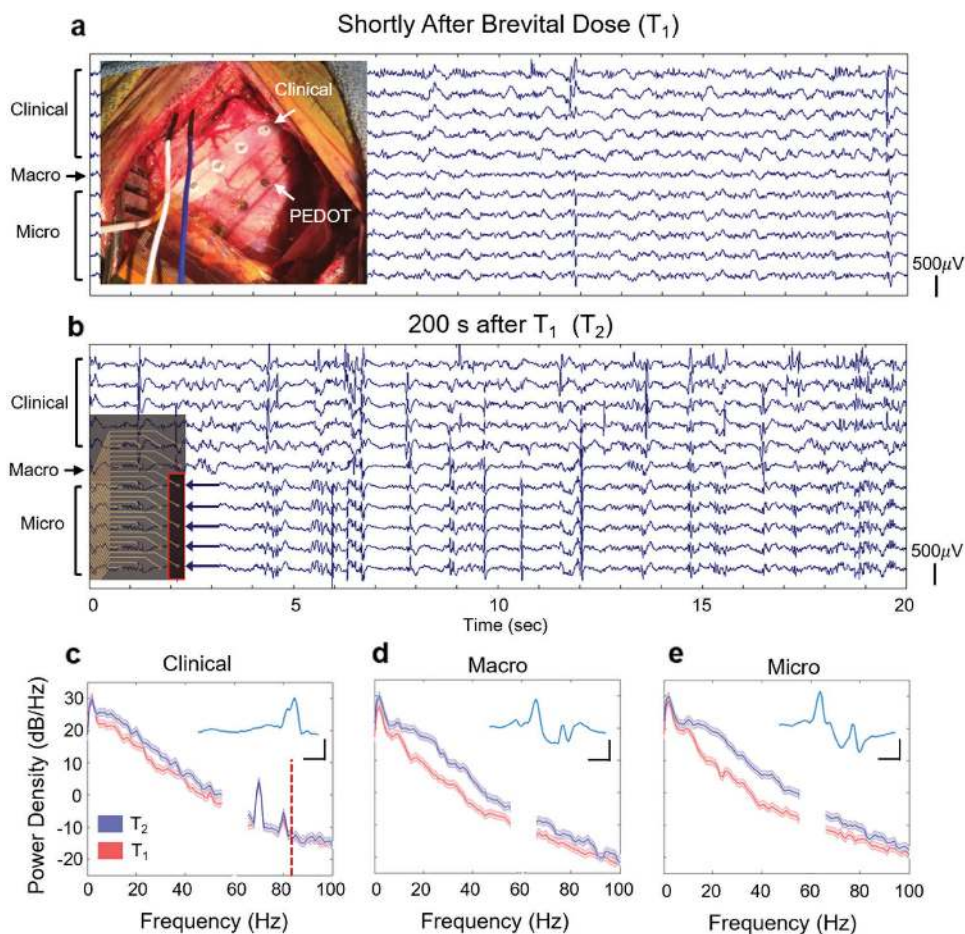**ADVANCED
FUNCTIONAL
MATERIALS**

www.afm-journal.de

Figure 4. Methohexital (Brevital) induced differences in clinical, PEDOT macro, and micro electrodes. a) Simultaneously captured ECoG traces from clinical, PEDOT macro, and micro electrodes shortly after Methohexital dose (T_1) and b) 200 s after T_1, (T_2). Inset in (a) shows the clinical and PEDOT ECoG probes implanted over the superior and middle temporal gyrus. Inset in (b) shows which microelectrodes are plotted for (a) and (b). Power spectral densities of a c) clinical, d) macro, and e) micro electrode taken from T_1 (red) and T_2 (blue). The dark blue and red lines are average PSD estimates from overlapping time windows and the lightly colored shaded regions are the 95% pointwise c.i. (see the Experimental Section). Power in the 10–50 Hz band show significant differences only for PEDOT electrodes: 0.010 (clinical), 5.5×10^{-6} (macro), and 4.3×10^{-6} (mirco) (Wilcoxon signed rank test). The noise spectra around 60 Hz frequency was filtered out with a notch filter for all devices. The dashed red vertical line in (c) indicates the upper passband cutoff frequency for the clinical system. Insets from (c)–(e) show an interictal epileptic discharge (IED) captured concurrently across the three electrode types. Scale bars are 200 µV (vertical) and 50 ms (horizontal).

when computing the difference in power for the 10–50 Hz band, only the PEDOT electrodes showed a significant difference. Again, the measured variation can also be explained by differences in neural activity across several centimeters of cortex. As with the previous subject, the PEDOT microelectrode shows a significant difference between baseline and increased epileptiform activity demonstrating their potential clinical utility.

To further examine spatial specificity, we analyzed stimulus-locked cognitive activity in two patients. Recordings were made from the anterior STG for S2 (**Figure 5**a) and from the posterior STG for S3 (Figure 5d) while each was awake for the clinical mapping of eloquent cortex. While awake, each also performed a short task (see the Experimental Section). S2 verbally responded on >95% of naming trials and S3 made a correct match/mismatch decision on 98% of trials.

Spectrograms demonstrated increases in high-frequency power specific to certain stimuli classes: auditory words for S2

(Figure 5c) and noise-vocoded stimuli for S3 (Figure 5f).[28] The most consistent difference across electrodes was in the frequency ranges commonly referred to as "high-gamma," here defined as 70–170 Hz (Figure 5c,f shows the responses for three neighboring example channels from each subject). This high-frequency band amplitude (HFB) is highly correlated with population neuronal firing rates.[29] To better assess this HFB response, we looked at the response averages across electrodes.

Of the 56 microcontacts, 42 in S2 and 34 in S3 were functional, as determined by impedance <60 000 ohms. While reference autoclave experiments here and in ref. [23] showed negligible influence on the microarray impedances (Figure 2), some of the microarray dots displayed higher impedances after transportation and autoclave by hospital personal as determined by impedance measurements just prior to the recordings and is attributed to issues in handling the arrays rather than the autoclave process itself. In S2, 16 of 42 good electrodes demonstrated a significant ($p < 0.05$ false-discovery rate corrected)
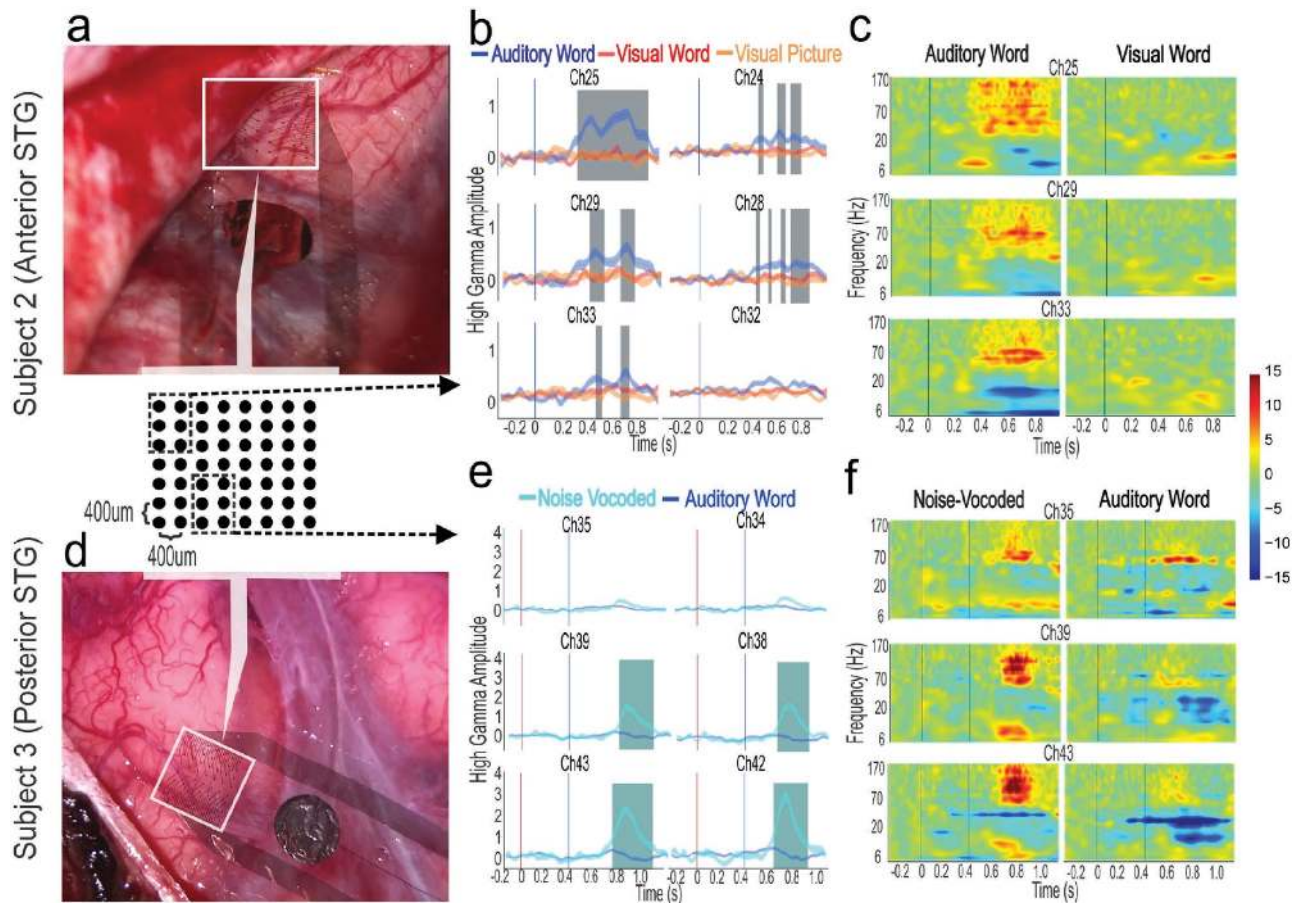
**ADVANCED
SCIENCE NEWS**
www.advancedsciencenews.com

**ADVANCED
FUNCTIONAL
MATERIALS**
www.afm-journal.de

Figure 5. Neural activity varies across distances as small as 400 µm. a,d) Electrode placement from the two subjects who performed cognitive tasks. Activity from six neighboring electrodes (3 × 2 electrodes) from the 8 × 7 electrode array is displayed to illustrate high-frequency amplitude variation. The white box highlights device placement (device partially obscured in subject 1 by the dural flap). b,e) High-frequency amplitude for the 3 × 2 channels confirming significant differences in Hilbert analytic amplitude from 70–170 Hz between stimuli classes (shaded regions are anova fdr-corrected significant differences). For subject 2, the blue vertical line indicates stimulus onset. For subject 3, the red vertical line indicates visual stimuli onset (to which no response was found across the electrodes) and blue line indicates auditory stimulus onset. c,f) Time–frequency plots from three of the example channels (3 × 1) in response to different stimuli classes demonstrating strong differences in higher frequencies. Displayed is trial-averaged power determined by wavelets.

increase to auditory words relative to visual words and pictures (38% of electrodes). In S3, 31 of 34 electrodes demonstrated a significant increase ($p < 0.05$ false-discovery rate corrected) to auditory noise-vocoded trials relative to human voice trials (91% of electrodes). S3 also saw a visual bigram prior to the auditory stimulus, but showed no significant response across electrodes to visual stimuli. Figure 5b,e shows the HFB of the six example electrodes chosen from a 3 × 2 portion of the grid, demonstrating that the presence of an effect and the variability of the effect size can vary across distances as small as 400 µm.

3. Discussion

Here we report the fabrication of a highly reproducible, high-yield PEDOT:PSS microarray, demonstrate PEDOT:PSS possesses superior impedance characteristics compared to Pt clinical electrodes, and show the first PEDOT:PSS recorded stimulus-locked human cognitive activity. A variety of structural

studies confim PEDOT:PSS is safe for implantation and our microaray had a high yield of functional microelectrodes (>96% functional) with a very narrow distribution of impedances. Microelectrodes measured similar electrophysiological phenomena as macrodots made of either PEDOT:PSS or Pt across anesthetized, awake, and pathological states despite the microelectrode's four orders of mangitude smaller area. The PEDOT micro-electrode exhibited significant differential power among various conditions (Figures 3 and 4) demonstrating their clinical viability. Finally, we demonstrated that the PEDOT:PSS microelectrode array was capable of resolving differences in cognitive responses across cortical tissue over distances as small as 400 µm.

In other cases, especially when considering the broad-band (1 Hz to Nyquist frequency) signals, PEDOT microelectrodes had highly similar signals as compared to the clinical electrodes as shown in Figure 4a,b. This can partly be attributed to referencing schemes (bi-polar vs uni-polar, see the Experimental Section), but is primarily a result of sensing signals much closer

**ADVANCED
SCIENCE NEWS**

www.advancedsciencenews.com

**ADVANCED
FUNCTIONAL
MATERIALS**

www.afm-journal.de

to each other (400 µm–3 mm vs 1–5 cm).[30] Recent work by Kellis et al. has shown that pairwise correlation from µEcoG electrodes is ≈0.5 with electrodes spaced 5 mm.[36] Since the maximum distance between any pair of microelectrodes in this work is 4.2 mm, the observed signal similarity is consistent with Kellis et al.

Measuring highly similar signals has advantages and disadvantages, which change depending on use case. An advantage for measuring highly similar or redundant signals is that they may help denoise a collective signal or feature when combined intelligently. For example, interictal epileptic discharges, IEDs, are difficult to detect using automated algorithms and even challenging for trained electrophyiologists. IED detection might be improved if there were multiple redundant views of the signal which could increase detection confidence. This concept has been used by electrophysiologists to better detect action potentials from single units (e.g., tetrode designs). This potential motivates investigation of high density or mixed density surface probe designs, even if sensed signals appear to be highly similar.[21b]

As electrode development pushes toward decreasing contact size to increase spatial specificity, PEDOT:PSS contacts facilitate high SNR recordings and have a number of favorable characteristics. The spin-casting approach used in our fabrication provides a consistent electrochemical interface and insignificant morphological changes post-sterilization.[23] This approach leads to a very high yield of functioning electrodes (>96%) with a narrow range of impedances. The EIS impedances for PEDOT:PSS are smaller than those for Pt which in turn results in lower noise power spectral density than those of Pt (Figure 2e,f). This difference is significant because cognitive processes that are generally observed at low frequencies (theta, gamma, and low frequency oscillations) need to be measured with the lowest possible electrode noise. Additionally, important information about neuronal firing in the high-frequency bands has a very low amplitude, making it critical to maximize SNR.

Combining these reliably low impedances with several other favorable characteristics makes PEDOT:PSS a strong contender for leading the next generation of neural electrochemical interfaces. These additional characteristics include high charge injection capacity (safe/efficient stimulation),[9] compliant mechanical properties for mimicking the curvilinear brain tissue and to compensate brain micromotion in order to reduce tissue damage,[10] and enhanced biocompatible electrode/tissue interfaces to minimize biofouling.[8a,11] With higher channel counts being achievable via passive wiring or active multiplexing, PEDOT:PSS presents a great opportunity to achieve high-density, high-SNR arrays, with greatly increased spatial specificity.

Despite the promise of PEDOT:PSS for neural recording, we are only aware of one group which displayed human neural recordings from a PEDOT:PSS device.[21] They demonstrated that PEDOT:PSS electrodes with an area of 10×10 µm^2 can sense a wide variety of neurophysiological activity including low-frequency oscillations (beta, delta, and spindle activity) and high-frequency action potentials. They validated these neurophysiological signals by showing they are modulated by other neurophysiological signals and coarse conditions such as awake or under a variety of anesthesia, similar to our results in

Figure 3. However, they have not demonstrated how the sensed neurophysiology is modulated by sensory stimulus or cognitive processing, which is one of the main contributions of this work. Interestingly, we did not detect action potentials, which may have been caused by excessive CSF between the pial surface and probe, which acts as a spatial low pass filter. In ref. [21b], they suggest adding openings homogenously throughout the probe to allow CSF to flow over the probe as well as minimizing the amount of CSF near the probe.[21b] Additionally, the device presented in our study has a larger electrode size (50 µm diameter vs 10 µm diameter), which may have prevented the electrodes from sensing action potentials. Finally, the neurogrid device makes use of a tetrode-like design, concentrating 4 electrodes every 2000 µm as opposed to our grid placing 1 electrode every 400 µm. Future studies will need to determine optimal electrode design, which will undoubtedly vary for different clinical and experimental questions.

Finally, we examined the ability of PEDOT:PSS microgrid arrays to measure stimulus-locked cognitive responses to audiovisual stimuli. Neural responses to stimuli showed increases in power in high frequencies, likely related to neuronal firing.[29] These increases proved to reliably discriminate different stimuli, both between language modalities (S2) and within a single language modality (S3). Further, the high-frequency amplitude and effects differed within a displacement of 400 µm, demonstrating the great spatial specificity possible with PEDOT:PSS microelectrodes.

4. Conclusion and Outlook

The utility of high-density, high-SNR arrays with high spatial resolution is straightforward within the context of basic science. PEDOT:PSS microarrays can extend the ability of intracranial research to identify precisely the borders of functional regions and tease apart the information processing microcircuitry operations within these regions. Perhaps more important is the great potential for PEDOT:PSS clinical applications as well and the potential for higher SNR and higher spatial resolution ECoG to improve patient outcomes for surgical brain resections. The current gold standard for sparing eloquent, motor, and sensory cortex during resections is direct cortical stimulation to map brain function. In addition to this gold standard, recent work demonstrates the potential use of recorded HFB activity as a complementary method for functional mapping.[31] The surgeon often faces a very difficult tradeoff of maximizing resection extent to remove pathological tissue and thus improves the patient's health, while preserving as much function as possible. The coarse spacing, limited channel count, and nonconformability of the currently used electrode substrate constrain the resolution of the information available to make a decision about this tradeoff. PEDOT:PSS electrodes provide safe and efficient stimulation in addition to their high-SNR recording ability and conformable characteristics. Using future arrays combining the excellent stimulation and recording capabilities of PEDOT:PSS, neurosurgeons would be more confident in the functional boundaries of the exposed cortex, and thus be able to make a more informed decision of which tissue to resect. Development of these arrays is facilitated by

**ADVANCED
SCIENCE NEWS**
www.advancedsciencenews.com

**ADVANCED
FUNCTIONAL
MATERIALS**
www.afm-journal.de

the fact that PEDOT:PSS electrode fabrication allows quickly iterated designs. Eventually, working together, surgeons and researchers will be able to develop arrays that are effective for optimizing post-surgical outcomes.[13–15]

5. Experimental Section

Device Fabrication: 4 inch glass wafers (Specialty Glass Products) were used as a substrate carrier for the thin parylene C layers. The glass wafers were first solvent cleaned by rinsing with acetone/isopropanol (IPA)/deionized (DI) water/IPA, then were subjected to ultrasonic agitation in IPA for 5 min, and were then rinsed again with acetone/IPA/DI water/IPA. Diluted Micro-90 (0.1%) as an antiadhesion layer was spun-cast at 1500 rpm on the glass wafer to facilitate the separation of the device after the device fabrication is completed. A first parylene C layer ($\approx$ 3 µm) was deposited by chemical vapor deposition using a PDS 2010 Parylene coater system. Metal lead patterns were defined and exposed using a Karl Suss MA6 mask aligner using NR9-3000 negative resist. Temescal BJD 1800 electron beam evaporator was used for the deposition of 10 nm Ti adhesion layer and 100 nm Au contact layer, and lift-off process in acetone followed. O_2 plasma (Oxford Plasmalab 80 RIE) was then applied for 2 min (150 W RF power) to activate the surface of parylene C for enhancing the adhesion of the subsequent encapsulating parylene C layer. A $\approx$ 3 µm parylene C layer was then deposited and followed by coating another Micro-90 antiadhesion layer. This time, a slightly higher concentrated Micro-90 (1% as opposed to 0.1% for the first layer) was spun-cast at 650 rpm for 10 s on this second parylene C layer for the ease of separation of the subsequent layers. A third parylene C layer was then deposited, followed by the spin-coating and patterning the thick 2010 SU-8 photoresist layer which developed with an SU-8 developer. O_2 plasma was used to etch the openings in the third and then second parylene C layers prior to the deposition of PEDOT:PSS. After the O_2 plasma etching step, the exposed Au surface was cleaned using moderate sonication while the device was immersed in DI water. 20 mL aqueous dispersion of PEDOT:PSS (PH 1000 from Clevios) was mixed with ethylene glycol (5 mL), dodecylbenzene sulfonic acid (50 µL), and 1 wt% of (3-Glycidyloxypropyl)trimethoxysilane, and the solution was spun-cast at 650 rpm for 30 s and pre-baked at 95 °C for 1 min. The third parylene C layer was then mechanically peeled off in all regions except where PEDOT: PSS made contact with the Au surface on the microarray and macrodot regions. Finally, the devices were cured at 140 °C for 1 h and immersed in DI water to remove any Micro-90 residue from the PEDOT:PSS and parylene C surface. Fabrication of the platinum microarrays followed similar procedure to that of PEDOT:PSS devices except for the PEDOT:PSS deposition which was not carried out. For the Pt devices, a 10 nm Ti adhesion layer and 100 nm Pt contact layer were deposited by sputtering (Denton Discovery 18 Sputter System).

Device Characterization: The devices were imaged using an FEI SFEG ultrahigh resolution SEM at 10 kV accelerating voltage and a magnification of with 4702X. To reduce electron charging in the specimen, a 15 nm thick Ti layer was deposited on the back of the device and that electrically connected to the stage of the system providing a runaway path for impinging electrons. A Veeco Scanning Probe Microscope was used to take AFM images in noncontact tapping mode. EIS was performed using a GAMRY interface 1000E in phosphate buffer saline solution, using three electrodes configuration, i.e., Ag/AgCl electrode as a reference, a large platinum electrode as a counter elelectrode, and PEDOT:PSS/Pt microarray/macrodot as the working electrode. Sinusoidal signals with 10 mV rms AC voltage and zero DC voltage were applied and the frequency was swept from 1 Hz to 10 kHz.

Electrophysiology Methods, Acquisition: Patients S1–S3 undergoing clinical mapping of eloquent cortex provided informed consent to have the microarray placed on their pial surface and to participate in a 10 min task. The PEDOT microarray was placed on the STG: anterior STG for S2 and posterior STG for S1 and S3. UC San Diego Health Institutional Review Board (IRB) reviewed and approved study protocol.

Patient S4 provided informed consent to have microarray placed on their pial while unconscious. The electrode was implanted on the lateral surface of the temporal lobe across the superior and middle temporal gyrus. The Partners Human Research Committee reviewed and approved the IRB protocol at Brigham and Women's Hospital.

S2 read visual words, repeated auditory words, and named visual pictures. S3 saw a three-letter string (GUH, SEE) and then heard an auditory two-phoneme combination, making a decision whether the visual and auditory stimuli matched. Interspersed were visual control trials in which a false font was followed by a real auditory stimulus and auditory control trials in which a real letter string was followed by a six-band noise-vocoded two-phoneme combination.

The clinic compatible, open source electrophysiology (ephys) system was used based on Intan technology (Los Angeles, CA) to record acutely during neurosurgery. The details of the system have been published[32] and the design files and software are freely available on https://github.com/TNEL-UCSD/nacq and are briefly discussed below.

The system was capable of recording 256 channels at 20 kHz and featured 5 kV RMS power isolation. The purpose of an isolator was to protect the patient from hardware malfunctions and/or power surges. The system consisted of an adapter, amplifier and digitizer (Intan RHD2164), power isolator, and USB buffering board (RHD2000). The adapter had switches, which could connect a subset of electrodes to reference (REF) or ground (GND). Typically, two macrodots were connected to REF while GND was connected to an external needle probe (The Electrode Store, Buckley, WA) that was inserted in the scalp near the craniotomy. The signals were then amplified and digitized by the RHD2164, passed through the power isolator, then buffered and sent via USB to a laptop.

Since ephys components were within several feet of the surgical site, these components were sterilized via standard methods at each of the participating hospitals. The adapter and RHD2164 were sterilized using an electronics friendly process called Sterrad. Sterrad was a low-temperature sterilization method that uses hydrogen peroxide plasma to eliminate microbes. It was found that there were no obvious effects to the hardware in the first three to five sterilization runs.

The clinical recording system was an Xltek with 128 channels (Natus Neurology, Pleasanton, CA). For patients S1–S3, the sampling frequency was 500 Hz (70 Hz cutoff) and for S4, it was 250 Hz (83.33 Hz cutoff). Clinical signals were referenced using a bi-polar configuration, which enhanced signal differences between recording channels. On the other hand, research electrodes were measured with a unipolar configuration which resulted in measuring signals with less differences.

Analysis and Statistical Methods: The following software and toolboxes were used: MATLAB, EEGLAB, and the Fieldtrip, Chronux toolboxes.

In Figure 3, power spectral densities were estimated using Welch's method (pwelch) using a Kaiser Window of length 0.75 s with $\beta = 4$. An entire time period of 10 s was used with 50% between windows. Pointwise c.i.s were computed using the Matlab pwelch function and the expression for c.i. was equation 5.3.64 on page 280 in Manolakis et al.[33] Power in the 10–50 Hz band was obtained by forward and reverse filtering the signal with a third-order IIR Butterworth filter and then the resultant was squared. To determine statistical significants, the two epochs were windows into 0.5 s nonoverlapping segments. Power was estimated for all windows across the two conditions and then run through Wilcoxon signed rank sum test to determine significance. The absolute median difference of the PSD estimate was computed over the 10–50 Hz to gauge separability across frequencies. The time–frequency plot was generated using short-time Fourier transform method with Slepian tapers (mtspecgramc from the Chronux toolbox). The moving window was of length 400 ms and step 40 ms. A time-bandwidth product of 5 and 5 tapers were used. The power was converted to units of dB then z-scored across to highlight temporal dynamics.

Figure 4 uses the same method to compute PSDs as Figure 3. The only difference was that a time period of 20 s was used.

For the analysis in Figure 5, the data were low-pass filtered at 400 Hz and then downsampled to 1000 Hz.[34] To remove noise, the average signal of the microdot electrodes was subtracted from each channel

(average re-reference) and each channel was then bandstopped around line noise and its harmonics. Next, the data were epoched to the onset of stimulus presentation (visual word/picture/auditory word onset for S2, visual word onset for S3) and for each trial the baseline from −300 to 0 ms was subtracted. Trials judged to have artifactually high amplitude or variances were removed from the data set. To investigate differences between stimulus classes in the high-frequency band, amplitude was obtained using a fourth-order Butterworth bandpass filter from 70 to 170 Hz and then taking the analytic amplitude from the Hilbert transform and smoothed with a moving window. ANOVAs were run between stimuli classes and corrected for multiple comparisons with false-discovery rate.[35] S2 had 60 trials for each condition (visual word, auditory word, visual picture). S3 had 157 trials for the human voice and 80 trials for noise-vocoded stimulus. For the time–frequency plots, epochs were transformed from the time domain to the time–frequency domain using the complex Morlet wavelet transform. For the HFB frequencies, constant temporal and frequency resolution across target frequencies were obtained by adjusting the wavelet widths according to the target frequency. The wavelet widths increased linearly from 14 to 38 resulting in a constant temporal resolution of 16 ms.

Data Availability: The data are available from the authors upon request by e-mail from the corresponding authors.

Supporting Information

Supporting Information is available from the Wiley Online Library or from the author.

Conflict of Interest

The authors declare no conflict of interest.

[1] G. Schalk, K. Miller, N. Anderson, J. Wilson, M. Smyth, J. Ojemann, D. Moran, J. Wolpaw, E. Leuthardt, *J. Neural Eng.* **2008**, *5*, 75.

[2] A. M. Dale, E. Halgren, *Curr. Opin. Neurobiol.* **2001**, *11*, 202.

[3] J.-P. Lachaux, N. Axmacher, F. Mormann, E. Halgren, N. E. Crone, *Prog. Neurobiol.* **2012**, *98*, 279.

[4] A. M. Taplin, A. de Pesters, P. Brunner, D. Hermes, J. C. Dalfino, M. A. Adamo, A. L. Ritaccio, G. Schalk, *Epilepsy Behav. Case Rep.* **2016**, *5*, 46.

[5] a) N. T. Sahin, S. Pinker, S. S. Cash, D. Schomer, E. Halgren, *Science* **2009**, *326*, 445; b) R. T. Canolty, E. Edwards, S. S. Dalal, M. Soltani, S. S. Nagarajan, H. E. Kirsch, M. S. Berger, N. M. Barbaro, R. T. Knight, *Science* **2006**, *313*, 1626; c) N. Mesgarani, C. Cheung, K. Johnson, E. F. Chang, *Science* **2014**, *343*, 1006; d) M. J. Vansteensel, E. G. Pels, M. G. Bleichner, M. P. Branco, T. Denison, Z. V. Freudenburg, P. Gosselaar, S. Leinders, T. H. Ottens, M. A. Van Den Boom, *N. Engl. J. Med.* **2016**, *375*, 2060; e) W. Wang, J. L. Collinger, A. D. Degenhart, E. C. Tyler-Kabara, A. B. Schwartz, D. W. Moran, D. J. Weber, B. Wodlinger, R. K. Vinjamuri, R. C. Ashmore, *PLoS One* **2013**, *8*, e55344; f) C. A. Chestek, V. Gilja, C. H. Blabe, B. L. Foster, K. V. Shenoy, J. Parvizi, J. M. Henderson, *J. Neural Eng.* **2013**, *10*, 026002.

[6] J. C. Horton, D. L. Adams, *Philos. Trans. R. Soc., B* **2005**, *360*, 837.

[7] B. Rubehn, C. Bosman, R. Oostenveld, P. Fries, T. Stieglitz, *J. Neural Eng.* **2009**, *6*, 036003.

[8] a) R. J. Vetter, J. C. Williams, J. F. Hetke, E. A. Nunamaker, D. R. Kipke, *IEEE Trans. Biomed. Eng.* **2004**, *51*, 896; b) G. Buzsáki, *Nat. Neurosci.* **2004**, *7*, 446; c) P. A. House, J. D. MacDonald, P. A. Tresco, R. A. Normann, *Neurosurg. Focus* **2006**, *20*, 1.

[9] a) S. F. Cogan, *Annu. Rev. Biomed. Eng.* **2008**, *10*, 275; b) D. R. Merrill, M. Bikson, J. G. Jefferys, *J. Neurosci. Methods* **2005**, *141*, 171; c) V. S. Polikov, P. A. Tresco, W. M. Reichert, *J. Neurosci. Methods* **2005**, *148*, 1.

[10] a) R. A. Green, R. T. Hassarati, J. A. Goding, S. Baek, N. H. Lovell, P. J. Martens, L. A. Poole-Warren, *Macromol. Biosci.* **2012**, *12*, 494; b) M. R. Abidian, D. C. Martin, *Adv. Funct. Mater.* **2009**, *19*, 573; c) S. F. Cogan, K. A. Ludwig, C. G. Welle, P. Takmakov, *J. Neural Eng.* **2016**, *13*, 021001.

[11] a) N. G. Hatsopoulos, J. P. Donoghue, *Annu. Rev. Neurosci.* **2009**, *32*, 249; b) C. E. Lagoa, J. Bartels, A. Baratt, G. Tseng, G. Clermont, M. P. Fink, T. R. Billiar, Y. Vodovotz, *Shock* **2006**, *26*, 592.

[12] a) E. W. Keefer, B. R. Botterman, M. I. Romero, A. F. Rossi, G. W. Gross, *Nat. Nanotechnol.* **2008**, *3*, 434; b) N. A. Kotov, J. O. Winter, I. P. Clements, E. Jan, B. P. Timko, S. Campidelli, S. Pathak, A. Mazzatenta, C. M. Lieber, M. Prato, *Adv. Mater.* **2009**, *21*, 3970; c) E. Seker, Y. Berdichevsky, M. R. Begley, M. L. Reed, K. J. Staley, M. L. Yarmush, *Nanotechnology* **2010**, *21*, 125504.

[13] a) J.-H. Kim, G. Kang, Y. Nam, Y.-K. Choi, *Nanotechnology* **2010**, *21*, 085303; b) M. Heim, B. Yvert, A. Kuhn, *J. Physiol.* **2012**, *106*, 137; c) S. Park, Y. J. Song, H. Boo, T. D. Chung, *J. Phys. Chem. C* **2010**, *114*, 8721.

[14] J. Rivnay, S. Inal, B. A. Collins, M. Sessolo, E. Stavrinidou, X. Strakosas, C. Tassone, D. M. Delongchamp, G. G. Malliaras, *Nat. Commun.* **2016**, *7*, 11287.

[15] a) R. A. Green, N. H. Lovell, G. G. Wallace, L. A. Poole-Warren, *Biomaterials* **2008**, *29*, 3393; b) M. R. Abidian, J. M. Corey, D. R. Kipke, D. C. Martin, *Small* **2010**, *6*, 421; c) X. Cui, V. A. Lee, Y. Raphael, J. A. Wiler, J. F. Hetke, D. J. Anderson, D. C. Martin, *J. Biomed. Mater. Res.* **2001**, *56*, 261.

[16] a) M. R. Abidian, K. A. Ludwig, T. C. Marzullo, D. C. Martin, D. R. Kipke, *Adv. Mater.* **2009**, *21*, 3764; b) K. A. Ludwig, J. D. Uram, J. Yang, D. C. Martin, D. R. Kipke, *J. Neural Eng.* **2006**, *3*, 59.

[17] D.-H. Kim, J. Viventi, J. J. Amsden, J. Xiao, L. Vigeland, Y.-S. Kim, J. A. Blanco, B. Panilaitis, E. S. Frechette, D. Contreras, *Nat. Mater.* **2010**, *9*, 511.

[18] M. R. Abidian, D. C. Martin, *Biomaterials* **2008**, *29*, 1273.

[19] L. Groenendaal, F. Jonas, D. Freitag, H. Pielartzik, J. R. Reynolds, *Adv. Mater.* **2000**, *12*, 481.

[20] a) M. Asplund, E. Thaning, J. Lundberg, A. Sandberg-Nordqvist, B. Kostyszyn, O. Inganäs, H. von Holst, *Biomed. Mater.* **2009**, *4*, 045009; b) D.-H. Kim, J. A. Wiler, D. J. Anderson, D. R. Kipke, D. C. Martin, *Acta Biomater.* **2010**, *6*, 57.

[21] a) D. Khodagholy, J. N. Gelinas, T. Thesen, W. Doyle, O. Devinsky, G. G. Malliaras, G. Buzsáki, *Nat. Neurosci.* **2015**, *18*, 310; b) D. Khodagholy, J. N. Gelinas, Z. Zhao, M. Yeh, M. Long, J. D. Greenlee, W. Doyle, O. Devinsky, G. Buzsáki, *Sci. Adv.* **2016**, *2*, e1601027.

[22] a) M. Sessolo, D. Khodagholy, J. Rivnay, F. Maddalena, M. Gleyzes, E. Steidl, B. Buisson, G. G. Malliaras, *Adv. Mater.* **2013**, *25*, 2135; b) D. Khodagholy, T. Doublet, M. Gurfinkel, P. Quilichini, E. Ismailova, P. Leleux, T. Herve, S. Sanaur, C. Bernard, G. G. Malliaras, *Adv. Mater.* **2011**, *23*, H268.

[23] I. Uguz, M. Ganji, A. Hama, A. Tanaka, S. Inal, A. Youssef, R. M. Owens, P. P. Quilichini, A. Ghestem, C. Bernard, *Adv. Healthcare Mater.* **2016**, *5*, 3094.

[24] J. Viventi, D.-H. Kim, L. Vigeland, E. S. Frechette, J. A. Blanco, Y.-S. Kim, A. E. Avrin, V. R. Tiruvadi, S.-W. Hwang, A. C. Vanleer, *Nat. Neurosci.* **2011**, *14*, 1599.

[25] M. Ganji, A. Youssef, A. Tanaka, V. Gilja, E. Halgren, S. A. Dayeh, unpublished.

[26] E. Huupponen, A. Maksimow, P. Lapinlampi, M. Särkelä, A. Saastamoinen, A. Snapir, H. Scheinin, M. Scheinin, P. Meriläinen, S. L. HIMANEN, *Acta Anaesthesiol. Scand.* **2008**, *52*, 289.

[27] a) W. A. Kofke, R. Tempelhoff, R. M. Dasheiff, *J. Neurosurg. Anesthesiol.* **1997**, *9*, 349; b) A. R. Wyler, E. Richey, R. A. Atkinson, B. P. Hermann, *Epilepsia* **1987**, *28*, 490.

[28] P. Souza, S. Rosen, *J. Acoust. Soc. Am.* **2009**, *126*, 792.

[29] S. Ray, N. E. Crone, E. Niebur, P. J. Franaszczuk, S. S. Hsiao, *J. Neurosci.* **2008**, *28*, 11526.

[30] a) M. W. Slutzky, L. R. Jordan, T. Krieg, M. Chen, D. J. Mogul, L. E. Miller, *J. Neural Eng.* **2010**, *7*, 026004; b) D. T. Bundy, E. Zellmer, C. M. Gaona, M. Sharma, N. Szrama, C. Hacker, Z. V. Freudenburg, A. Daitch, D. W. Moran, E. C. Leuthardt, *J. Neural Eng.* **2014**, *11*, 016006.

[31] F. Darvas, R. Scherer, J. G. Ojemann, R. Rao, K. J. Miller, L. B. Sorensen, *NeuroImage* **2010**, *49*, 930.

[32] J. Hermiz, N. Rogers, E. Kaestner, M. Ganji, D. Cleary, J. Snider, D. Barba, S. Dayeh, E. Halgren, V. Gilja, presented at *2016 IEEE 38th Annual International Conference of the Engineering in Medicine and Biology Society (EMBC)*, August 16-20, Orlando, FL **2016**.

[33] D. G. Manolakis, V. K. Ingle, S. M. Kogon, *Statistical and Adaptive Signal Processing: Spectral Estimation, Signal Modeling, Adaptive Filtering, and Array Processing*, Artech House, Norwood, MA **2005**.

[34] R. Oostenveld, P. Fries, E. Maris, J.-M. Schoffelen, *Comput. Intell. Neurosci.* **2010**, 2011.

[35] Y. Benjamini, Y. Hochberg, *J. R. Stat. Soc., B* **1995**, 289.

[36] S. Kellis, L. Sorensen, F. Darvas, C. Sayres, K. O'Neill III, R. B. Brown, P. House, J. Ojemann, B. Greger, *Clin. Neurophys.* **2016**, *127*, 591.